Nanofluid spray cooling characterization combining phase Doppler anemometry with high-speed visualization and thermography

Miguel Silva Figueiredo
miguel.s.figueiredo@tecnico.ulisboa.pt

Instituto Superior Técnico, Universidade de Lisboa, Portugal

October 2020

Abstract

The spray-wall interactions depict thermo fluid dynamics phenomena exploited in a vast range of applications, from internal combustion engines, electronic components cooling, HVAC, to numerous medical and industrial applications. Additionally, climate change awareness cries for the urgent development of more efficient and more climate-friendly cooling systems. For these reasons, the scientific community has been showing an interest in uncovering nanofluid possible applications. As they possess superior thermal conductivity and overall better thermal cooling performance, their potential use as a coolant has become a great promise.

In this order, nanofluids with gold and silver nanoparticles, with different geometries and concentrations ranging from 0.1 - 1 (wt.%) were atomized and characterized. The study performed on this dissertation adopted a novel combination of three techniques little exploited in the literature. The phase Doppler anemometry system and the synchronization of a high-speed camera with a high-speed thermographic infrared camera were used to describe spray impact onto the heated surface.

According to the results, a decreased surface tension and higher impingement distance favour heat transfer from the wall, as the wetted area increased. Moreover, changes in the thermophysical properties were noted with the addition of nanoparticles, when compared to the base fluid. Although their presence did not affect the spray dynamics, an increase of 9.8% to 21.9% of the maximum heat flux was noted during impact when compared to the base fluid.

Keywords: Spray cooling, Nanofluid, Time Resolved Infrared Thermography, Phase Doppler Anemometry

1. Introduction

Over the last few years, the development of the electronic systems, mainly in processing electronics, urges for the development of high heat flux removal systems. Cooling systems must assure the good functioning and endurance of these systems that are becoming more power concentrated due to aggressive miniaturization. The use of liquids has become an inevitable response, whether in single or two-phase liquid cooling, as heat dissipation from supercomputer chips approached $100W/cm^2$ [1, 2].

The most used liquid cooling systems come from pool boiling, channel or microchannel flow boiling, jet-impingement and spray cooling. Each approach has its own advantages, nevertheless, spray cooling is considered by some authors as the most advantageous (e.g. [1]). In ideal conditions, spray cooling achieves a heat flux removal in the order of $1200W/cm^2$, an order of magnitude higher than pool boiling, which only achieves $140W/cm^2$. When compared with jet-impingement, spray cooling offers better spatial cooling uniformity, that otherwise would be detrimental to some devices, resulting in higher cooling efficiencies and lower liquid consumption [2, 3].

In a simple way, spray cooling is obtained by the impact of the spray on the surface/element to cool. The spray is globally composed by numerous droplets within a wide range of sizes and velocities, which are generated at the nozzle, where the liquid breaks up due to instabilities, caused by its momentum. A spray, however, cannot be simply modelled as a sum of individual droplets, since there are numerous interactions between the droplets, with the air, and at impact with droplets previously

spread on the surface as well as with a possible deposited liquid film, also resulting from earlier spray injection. However, spray cooling, due to its complexity, still lacks theoretical modelling when compared to other cooling techniques. It is considered that spray cooling is limited by the cooling effectiveness of the conventional refrigerants, such as water, engine oil or ethylene [4].

Therefore, large interest by the scientific community regarding the scrutiny of nanofluid applications in cooling over the last few years is easily noticed. These nanofluids come with the promise of achieving higher heat transfer efficiencies, due to their enhanced thermal conductivity, when compared with conventional cooling fluids, whose properties largely enhance their cooling performance [5, 6].

Nanofluids are composed of solid particles that are dispersed in a base liquid (e.g. Water, Refrigerant Oils). These particles can be metallic (e.g. Aluminum, Gold, Silver) or nonmetallic (e.g. Carbon and Nitrides), whose dimensions are in the nanometer range $(10-100nm)$ [7]. Since nanoparticles have higher thermal conductivities, at least two orders of magnitude higher than their base liquid, they enhance the fluid's overall thermal conductivity. Additionally, other fluid-dynamic characteristics are stated in various studies, such as Brownian movement and higher fluid stability that should prevent particle settlement [6].

Nevertheless, controversial conclusions regarding the increase of the thermal conductivity and its contribution to enhance or worsen heat transfer can be found in the literature. In one hand, this means that more studies and more detailed analysis are still needed [6, 4]. On the other hand, there are other properties such as viscosity and local wettability, which can be strongly affected by the addition of the nanoparticles to the base fluids, altering the hydrodynamic characteristics of the flow, in complex processes which are still far to be accurately described.

In this regard, in order to diminish the existing gaps in this topic, this study is aimed at correlating the nanoparticle presence in the base fluid and its effect on thermophysical properties. Therefore, its influence on the atomization process and heat transfer is analyzed at two impact distances and at two initial surface temperatures. This study is a followup to a previous study [8], and it considers nanofluids with different nanoparticle chemical element, geometry and concentration. The atomization and heat transfer process are characterized using a novel combination of three techniques: phase Doppler anemometry and high speed visualization imaging, coming from a high speed camera and a thermographic camera.

2. Background

2.1. Nanofluid properties

To evaluate the thermal conductivity, the classical computation approach will be adopted. Considering well-dispersed solid spherical particles on a continuum medium, the thermal conductivity is given by:

$$K_{nf} = \frac{2K_{bf} + K_p + 2\phi\left(K_p - K_{bf}\right)}{2K_{bf} + K_p - \phi\left(K_p - K_{bf}\right)} K_{bf} \qquad (1)$$

where ϕ is the volume fraction of the solid particles, K_{bf} and K_p the base fluid and solid particle thermal conductivity, respectively, and considering them as bulk materials.

However, when considering different particle shapes, the introduction of an empirical shape factor (n) that relates the particle sphericity is needed, resulting in Equation (2). The shape factor is the ratio of the surface area of the non-spherical nanoparticle to that of an equivalent spherical nanoparticle with the same volume ($n = S/S^{'}$).

$$K_{nf} = \frac{K_p + (n-1)\,K_{bf} - (n-1)\,\phi\left(K_{bf} - K_p\right)}{K_p + (n-1)\,K_{bf} + \phi\left(K_{bf} - K_p\right)} K_{bf} \qquad (2)$$

The specific heat (c_p) is another fundamental property. It is mainly estimated based on heat equilibrium. According to Xuan and Roetzel (2000), c_p can be estimated as:

$$c_{p_{nf}} = \frac{(1-\phi)\left(\rho c_p\right)_{bf} + \phi\left(\rho c_p\right)_p}{(1-\phi)\,\rho_{bf} + \phi\rho_p} \qquad (3)$$

Finally, the specific mass (ρ) is calculated as:

$$\rho_{nf} = (1-\phi)\,\rho_{bf} + \phi\rho_p \qquad (4)$$

3. Experimental setup and procedures

3.1. Experimental Setup

The experimental arrangement used in the present work is schematically represented in Figure 1. The fluids under study were atomized and characterized by two distinct system arrangements. The underlined area of the scheme represents the main components of the experimental arrangement that includes the atomizer and the impact surface.

The atomizer (fig. 1, index 1) is composed of two parts: the swirl nozzle and the nozzle support that receives the liquid tangentially. The swirl nozzle has a discharge orifice of 0.42 mm in diameter and two opposing tangential ports with a squared shaped cross-section of $0.6 \times 0.6mm^2$. Detailed geometrical specifications can be found in [8].

The continuum liquid stream comes from a $3dm^3$ cylindrical reservoir (fig. 1, Reservoir 1), that is pressurized by air. The pressurization (relative)

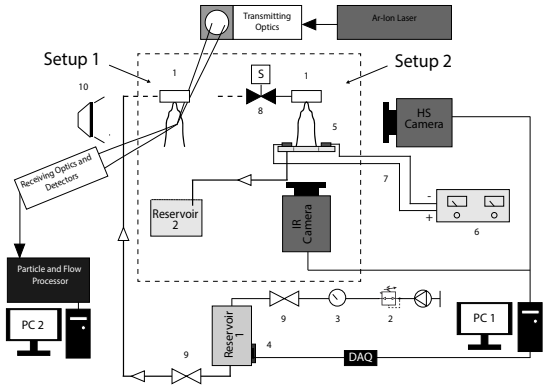

Figure 1: Experimental installation scheme: (1) Atomizer; (2) Air pressure regulator; (3) Manometer; (4) Temperature sensor; (5) Impact surface; (6) Power supply; (7) Electric cables; (8) Solenoid valve; (9) Manual valve; (10) Light source

was maintained at $87psi$ ($\pm 0.5psi$) by a IR1M Monnier compressed air regulator from Spirax Sarco (fig. 1, index 2) and monitored by a manometer (fig. 1, index 3).

Additionally, a K-type thermocouple (C03-K from Omega, fig. 1, index 4) was mounted on Reservoir 1 and it was connected to a data acquisition board DT9828 from Data Translation (fig. 1, DAQ) to measure the liquid's initial temperature.

A Phase Doppler Anemometry - PDA system was used to characterize the velocity and size of the droplets that constitute the spray, in various points of interest. This system was utilized in Setup 1 and it is composed by a $300mW - 400mW$ Ar-Ion Laser, from Spectra-Physics, a transmitting/receiving optics connected to a particle and flow processor (BSA P80, from Dantec Dynamics).

In Setup 2, the heat exchange between the spray and the heated surface was analyzed. A metallic base (fig. 1, index 5) paired with a thin stainless steel (AISI 304) surface was used to characterize the spray impact phenomena. This surface had a thickness of $20\mu m$ and was heated by Joule effect using a continuous current power supply (HP 6274B DC, fig. 1, index 6). Additionally, as this surface was very thin, the temperature variations at its inferior face were captured by a high-speed infrared (IR) thermographic camera (Onca-MwIR-InSb-320, from Xenics). Moreover, a solenoid valve (SV3108 from Omega, fig. 1, index 8) was mounted before the nozzle to improve the repeatability of the tests performed with the thermographic camera.

In both setups, a high-speed (HS) camera (Phantom v4.2) was mounted perpendicularly to the spray, allowing not only the capture of the free spray (used in Setup 1) but also the spray impact onto the heated surface (used in Setup 2). Along with this camera, a light source of 50 Watts with a diffusing glass (fig. 1, index 10) was mounted on the opposite side of the spray to improve the capture contrast. It is important to emphasize that both (HS and IR) cameras were synchronized for spray impact on Setup 2.

To finalize, after atomization the working fluids were redirected to a reservoir (fig. 1, Reservoir 2), where they are filtered and reutilized afterwards. It is worth mentioning that the most relevant thermophysical properties of all the nanofluids used here were evaluated before and after the experimental tests (i.e. before and after atomization). Changes in these properties were observed to be negligible, which supports the argument that there were no significant particle losses in the liquid feeding system or the atomizer, in agreement with a previous study [8].

3.2. Nanofluid Preparation and Characterization

One of the key aspects of the preparation of a nanofluid is to guarantee its homogeneity and stability. In this regard, the addition of a surfactant is advised and, in this context, the use of Cetyltrimethylammonium bromide (CTAB) was adopted. However, one of the downsides of the use of surfactants, including CTAB, is their impact on the liquid's surface tension. Additionally, as different nanoparticle concentrations were going to be used in this study, different surfactant concentrations were required to assure the homogeneity of the nanofluids at higher nanoparticles concentrations. Therefore, the first step was to establish a range of surfactant concentrations and analyze their effect on Deionized (DI) Water surface tension. To that end, different concentrations of DI Water-CTAB mixtures ranging from $0.01 - 1$(wt.%) were prepared and sonicated. Their surface tension was measured, and their values are represented in Figure 2.

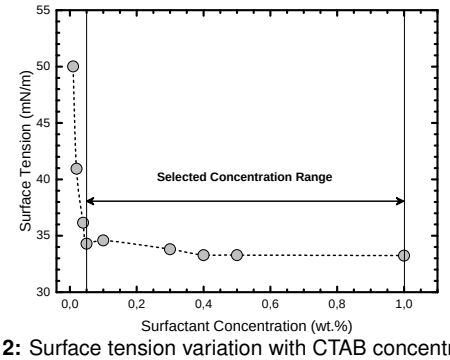

Figure 2: Surface tension variation with CTAB concentration in DI Water

From Figure 2, a rapid decrease of the surface tension is evident for very low surfactant concentrations (e.g. $<$ 0.04(wt.%)). However, the surface tension value stays constant above 0.04(wt.%), with variations lower than 3.2%. Therefore, the surfactant concentration range was fixed between

0.05 - 1(wt.%).

Afterwards, the nanofluids were prepared at the Structural Chemistry Center of the Department of Chemical Engineering at IST. These were supplied with different nanoparticle concentrations in the range of 0.1 - 1 (wt.%), mixed with DI Water containing surfactant. Thereafter, these were sonicated using a tip sonicator processor (UP200Ht from Hielscher), for 20 minutes on average at a mean amplitude of 40%. This ensured a good nanofluid homogeneity, as the majority of the nanofluids under study did not show apparent nanoparticle deposition for over a week. However, to avoid nozzle clogging, they were sonicated exactly before use.

The main characteristics and thermophysical properties for all the fluids used in this study, measured as described in the following paragraphs, are summarized in Table 1.

The thermal conductivity, specific mass and specific heat, were theoretically calculated based on their nanoparticle chemical element and concentration, following the Equations (1) to (4).

Viscosity was measured by the Structural Chemistry Center of the Department of Chemical Engineering, using a rheometer (A instruments ARI 500 ex) at room temperature ($20°C$).

Surface tension was measured with an optical tensiometer THETA, from Attension. The pendant drop method was used under controlled room temperatures ($20 \pm 3°C$). For each solution, 15 measurements were performed and averaged.

The refractive index was also evaluated since it is a fundamental input parameter for the PDA system. This property was evaluated with an Abbe refractometer (model 60/ED) with a Sodium D1 (yellow) light source at Faculdade de Ciências da Universidade de Lisboa. These measurements were conducted at a controlled temperature ($20 \pm 0.1°C$), using a thermostatic bath. This procedure was repeated for all the fluids under study following the user's manual instructions.

The surfaces used for impact were characterized in terms of wettability for all the liquids used. The static contact angle was obtained from an average of 5 measurements in 5 different locations of the stainless-steel surface, using an optical tensiometer THETA (from Attension) with the sessile drop method. These measurements are also represented in Table 1.

3.3. Methodologies and post-processing

3.3.1 Spray cone angle - SCA measurements

The high-speed camera was used to record the spray morphology. The videos were captured at $13\ 029 frames/second$, with a resolution of $192 \times 192 pixel^2$ and using an exposure time of $10\mu m$. A maximum and minimum spatial resolutions of $54.5\mu m/pixel$ and $70.6\mu m/pixel$ were obtained.

After this procedure, the recordings were exported to 8 bits greyscale jpeg images. Then, these images are processed and analyzed by a MATLAB routine to compute the spray cone angle (SCA). The first step regards the image contrast enhancement and then the image background is removed to reduce image noise (fig. 3(b)). Afterwards, the interest zone is manually selected and a greyscale threshold is applied, converting the image into a binary one (fig. 3(c). The final step creates a matrix with the left and right coordinates for each Z_i, that will be used as an input on the SCA expression. The fig. 3(d)) is just an overlap of the original image with the final.

(a) Step 1 (b) Step 2 (c) Step 3-4 (d) Overlap

Figure 3: Spray cone angle: image processing steps

Thereafter, with the coordinates of each boundary, the spray cone angle is calculated following Equation (5), that is based on triangles similarity:

$$SCA(°) = 2\tan^{-1}\left(\frac{x_1 - x_i}{2Z_i}\right) \tag{5}$$

where x_1 is the horizontal pixel difference between the left and right boundaries at the 1^{st} pixel of the zone of interest; x_i is homologous to x_1, but at the i^{th} pixel; Z_i is the vertical difference between the 1^{st} and the i^{th} pixel.

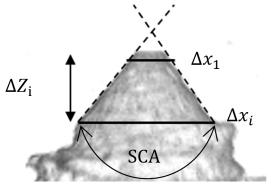

Figure 4: Spray cone angle scheme

It should be noted that the zone of interest for the SCA calculation corresponds to the stabilized zone of the spray liquid sheet (before the liquid sheet breakup). In these conditions, 90 different angles are measured for each video frame, where the first angle is measured 10 pixels under Z_1, to decrease the maximum absolute error. After the computation of those angles, the measurements for one video frame are averaged. This process is repeated for the rest of the video frames. The SCA measurements are represented in Table 1, with their respective standard deviations.

Table 1: Thermophysical and wettability properties

Element	DI Water	Base Fluid	Gold			Cylinders	Silver
Geometry	-	-	Spheres			Cylinders	Triangles
Mean Dimensions [nm]	-	-	Diameter: 80			Diameter: 12 Length: 39	Length: 30 Width: 17
Nanoparticle [$wt.\%$]	-	-	0.1	0.5	1	0.1	0.5
Surfactant [$wt.\%$]	-	0.05	0.5	0.05	0.05	0.5	0.05
Dynamic Viscosity [cP]	1.002	1.003	1.022	1.038	1.041	1.135	1.038
Specific Mass [Kg/m^3]	998.21	998.71	999.16	1002.94	1007.68	999.16	1002.73
Surface Tension [mN/m]	76.34	34.29	33.11	37.75	37.72	32.67	37.30
Specific Heat [$KJ/(KgK)$]	4.18	4.18*	4.18	4.16	4.14	4.18	4.16
Thermal Conductivity [$W/(mK)$]	0.60	NA	0.61	0.65	0.70	0.61	0.65
Static Contact Angle [º]	97.55	62.81	53.38	58.10	58.92	51.52	58.77
Spray Cone Angle [º] @$87psi$	73.64	73.45	73.26	74.40	75.28	73.62	74.97

Regarding the uncertainties, they were only attributed to the uncertainty of the spray boundaries. Hence, a maximum error associated with their location was defined to be ± 2 pixel. In this regard, a maximum error of $8.43°$ was computed.

3.3.2 Phase Doppler Anemometer measurements

Droplet size and velocity distributions were measured using a two-component Phase Doppler Anemometer. This system was used with the BSA Flow Software v5.10 and its optical configuration and validation parameters are summarized in Table 2. It should be noted that the particle and flow P80 processor performs 1D measurements. Therefore, the normal velocity component U was evaluated, given its importance in the empirical impact correlations used to predict the droplet impact outcomes.

Table 2: Phase Doppler optical configuration and validation parameters

Transmitting optics		**Receiving optics**	
Laser Power	300-400 mW	Scattering angle	69º
Beam wavelength	514.5 nm	Focal length	500 mm
Beam Spacing	60 mm	**Processor parameters**	
Focal length	310 mm	Spherical Validation	10%
Frequency shift	40 MHz	S/N Validation	-3dB

The measurements were performed at a distance of 10 mm and 20 mm, which are correlated to the first and second atomization moments [8], from the atomizer. The measured points consist of a radial grid, where $r = 0\ mm$ corresponds to the radial origin of the spray axis. Initially, two sets of measurement grids were adopted: $-20\ mm < r < 20\ mm$ (for $Z = 20\ mm$) and $-12\ mm < r < 12\ mm$ (for $Z = 10\ mm$) in 2 mm steps for two perpendicular axes, as shown in fig. 5.

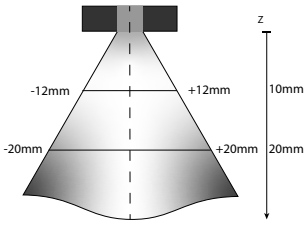

Figure 5: Measurement grid used with the phase Doppler system and coordinate system used.

The droplet size and velocity measurements were exported from the BSA Flow Software and were processed using a MATLAB routine. Moreover, the referred distributions were characterized by the arithmetic mean diameter (D_{10}), defined as:

$$D_{10} = \frac{\sum D_i}{\sum N_i} \tag{6}$$

where D_i corresponds to the validated droplet diameter and N_i to the number of validated droplets.

3.3.3 Heat flux and wetted area measurements

Regarding the impact surface, an AISI 304 stainless steel sheet with a predetermined area of $90 \times 60mm^2$, with a thickness of $20\mu m$, was used. This surface was fixed to a metallic frame using high-temperature silicone to reduce heat conduction losses and to prevent electrical contact. The bottom side of the surface was painted in black with an emissivity (ϵ) of 0.95. Then, Kapton tape was applied on the surface edges to stretch it, and two rectangular copper electrodes were soldered

in opposite sides of the sheet. The final step was to screw the metallic frame to the support, that collects and redirects the atomized liquid from the surface to the Reservoir 2, as represented in Figure 6.

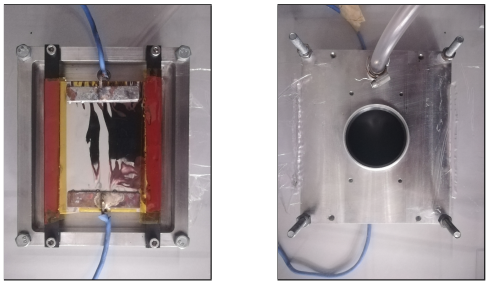

(a) Top view (b) Bottom view

Figure 6: Metallic support with the stainless steel sheet surface

The high-speed thermographic camera Onca-MwIR-InSb-320 (Xenics) was used to evaluate the heat transfer at the surface bottom face. This camera followed a custom-made calibration curve for an iteration time of $200\mu s$, defined in a previous study [9] and converts Analog-Digital Units into temperatures in Celsius. In this way, the thermographic camera recorded at $495 frames/second$ with a resolution of $230 \times 250\ pixel^2$, that resulted in a spatial resolution of $222.22\mu m/pixel$.

The high-speed camera recorded the spray impact, inferring important spray dynamics characteristics. Here, this camera was used at $990 frames/second$, which corresponds to two times the frame rate of the thermographic camera recordings, with an exposure of $10\mu s$. The adopted resolution varied from the impact conditions: for $Z = 20mm$, a $520 \times 320 pixel^2$ resolution was used, whereas, for $Z = 10mm$, a resolution of $520 \times 256\ pixel^2$ was adopted. In both cases, a spatial resolution of $64.49\mu m/pixel$ was obtained.

The spray cooling experiments were also performed at two different impingement heights, using two different initial surface temperatures $T_0 = \{74°C; 145°C\}$. It should be noted that each experimental condition was repeated at least 3 times. As the surface was heated by Joule effect, these temperatures correspond to the imposed currents of $I = \{9A; 15A\}$, resulting in the imposed heat fluxes of q''_0= $\{855\ W/m^2; 2375\ W/m^2\}$.

The computation of the removed heat fluxes from the surface was made using a MATLAB script and it considers a 2-dimensional pixel by pixel energy balance. A detailed description is available in [9]. From the tested conditions, a maximum uncertainty of $0.55°C$, regarding the temperature resolution, was computed and it corresponds to a maximum relative error of 2.70%.

An evaluation of the wetted area of the surface was also performed. It considers a threshold temperature that is based on the maximum spatial temperature derivative across the horizontal coordinate. It is mainly located at the two-pixel interface between the new wetted interface and the still dried area and is computed by their mean temperature.

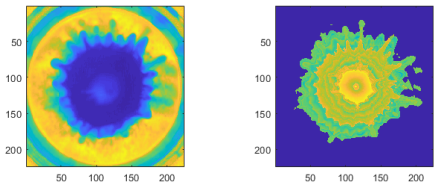

(a) Original image (b) Processed image

Figure 7: Wetted area computation demonstration

4. Results & discussion

4.1. Nanoparticle effect on fluid properties

The nanofluids used in this study contain nanoparticles and are composed of different weight concentrations, chemical element and shape. From Table 1, it is clear that the nanoparticle addition induces small variations in the thermophysical properties of the resulting nanofluids when compared with the base fluid.

Higher particle concentration leads, as expected, to an increase in specific mass and thermal conductivity, whereas an opposite trend is observed for the specific heat. The thermal conductivity expresses a major enhancement when compared with DI Water, showing an increase up to 16.3% for the highest gold nanofluid concentration. These observations are in good agreement with [10, 11]. The addition of the nanoparticles has a negligible effect in the value of the refractive index.

The dynamic viscosity increases with the presence of nanoparticles.This trend is in agreement within other studies (e.g. [6, 11]). When comparing the lowest concentration of gold nanofluids, one can confirm that the cylindrically shaped nanoparticles, although smaller in size, induce a major increase on the dynamic viscosity when compared with the nanospheres.

It is detected that the surfactant plays a dominant role in the surface tension value, deeply lowering it. From Table 1, the decrease of surface tension decreases the static contact angle values, which enhances the surface wettability. Nevertheless, when adding nanoparticles, the surface tension slightly increases when compared to that of the base fluid, as opposed to the observations made in [4]. However, between different nanoparticle materials and concentrations, the surface tension values were hardly modified. This was also postulated in [8].

Regarding the SCA measurements, the addition of nanoparticles did not exert any influence outside the margin of uncertainty.

4.2. Droplet size and velocity analysis before impact

As the spray under study represented overall good symmetry and axis independence, the measurement grid was reduced to the positive radial positions in one axis. In this order,the droplet mean diameter (D_{10}) and the normal mean velocity component (U) for Z= {10; 20} mm are represented in Figure 8.

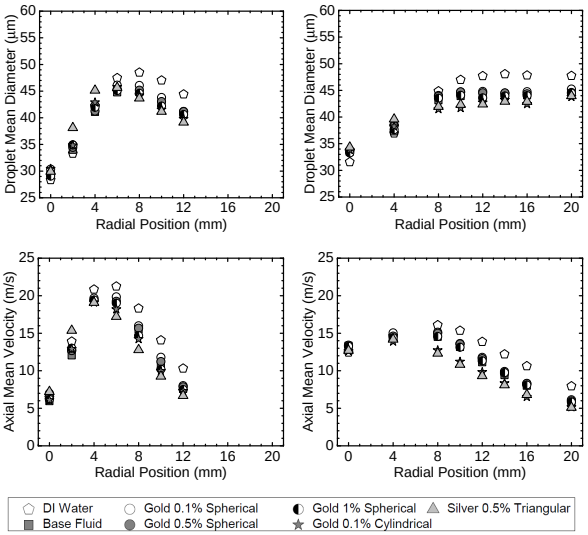

Figure 8: Droplet mean characteristics measured with the PDA at different radial positions.The left column corresponds to Z=10mm, while the right column to Z=20mm.

The smallest and slowest droplets are found at near centre of the spray (r= 0 mm) and are related to the spray swirling motion and its hollow pattern. Therefore, these droplets are transported to the centre due to the swirling motion, as they possess a lower mass. For Z=10mm, as the radial distance increases, the droplet diameter and velocity increases until 6 mm $<$ r $<$ 8 mm. For $r > 6mm$, both values of D_{10} and U decrease as the droplets start to interact with the surrounding air mass at a lower velocity.

Increasing the vertical distance (Z) to 20 mm, a similar D_{10} and U behaviour is observable. However, for this case, the interaction with the surrounding air is given at $r = 8mm$.

Performing a qualitative comparison between liquids with different surface tension, the decrease of this value decreases the droplet mean diameter, which in turn decreases the axial velocity (U). These observations reinforce that surface tension plays a major role in atomization (for the same viscosity value). Hence, the liquid sheet breakup generates more droplets, since the energy needed to increase the liquid surface area decreases.

The addition of nanoparticles to the base fluid did not affect the values of diameter/velocity, with only a few exceptions for Z=20mm (e.g. silver nanotriangles and gold nanorods). It should be noted that these exceptions can be attributed to experimental error or spray instabilities.

4.3. Impact predictions

Figure 9 represents the occurrence of the various droplet impact outcomes according to Bai et al. (2002) for a wetted surface at r=20mm and Z=20mm. From the previous subsection, the addition of the surfactant slightly decreased the mean diameter and velocity, which in turn slightly decrease the Reynolds number, and increase the Weber number, as surface tension decreased. These opposing trends will increase the Ohnersorge number (Oh). Therefore, higher values of the Ohnesorge number should correspond to slightly lower values of the Reynolds number, considering isolated droplets. In this order, this should induce a vertical displacement of the Oh-Re distribution for those fluids relatively to DI Water. Hence, the outcome of droplet impact will slightly change to the splash regime, as seen in fig. 9.

Regarding the effect of the addition of the nanoparticles, there are no observable changes within this range of concentrations when compared to the base fluid. This observation is a good indicator that spray dynamics and impact outcomes are unaffected by nanoparticle presence in the base liquid.

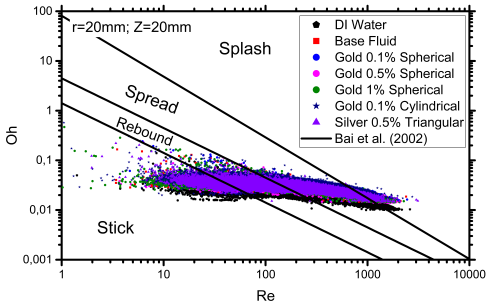

Figure 9: Impact outcomes prediction for the considered fluids (r=20mm; Z=20mm)

4.4. Heat transfer analysis

Figure 10 represents relevant captured instances during wall impact using the IR camera and HS camera. IR images also show the temperature distribution across the radius, with an impact distance of 10 mm and an initial surface temperature of $145°C$.

The frame before liquid contact sets t_0, where the initial temperature is at a constant temperature. At 2ms, the initial contact is made, and the spray is just a thin liquid structure, far from developed. At t=8ms, although roughly visible, the spray starts to form a hollow liquid sheet and some disruptive ligaments start to be visible. Hence, the formation of the first droplets, due to liquid sheet breakup and due to impact, start to arise. At 28ms, an almost

closed hollow smooth liquid sheet, contracted by surface tension forces, is formed. One can qualitatively say that the droplets, resulting from splash or primary atomization, become smaller.

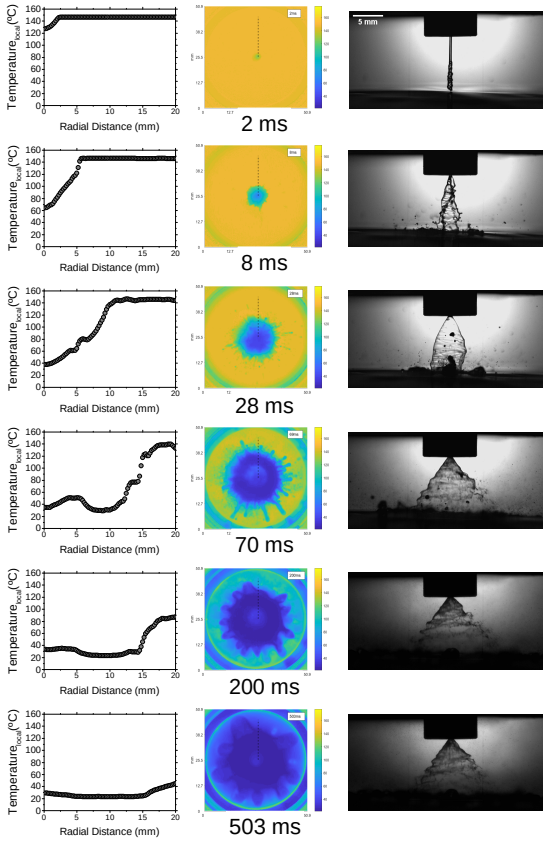

Figure 10: a)Temperature variation along the radial profile (identified in the IR images by the black dashed line) during spray impact on the heated surface, b) IR images taken from the backside of the surface, synchronized with c) Side views (taken with the high-speed camera) of the spray showing its dynamics for DI Water. (q"=2375W/m^2, $Z = 10mm$)

As the velocities increase, at 34ms, the surface tension forces do not hold the closed bubble, as it starts to straight the cone, becoming almost developed. Also, at this point, a major part of the analyzed surface area is wetted by the impacting liquid, forming a liquid film, due to deposition. Hence, the overall removed heat fluxes become maximum, as the active cooling area or film liquid line front becomes higher. At later time intervals ($t > 70ms$), as the temperatures and heat fluxes start to stabilize, the formation of secondary droplets at the edges of the spray intensifies.

4.4.1 Effect of the surface initial temperature

The cooling transient curves for two different imposed heat fluxes are shown in Figure 11(a) and Figure 11(b), for $q''_{imp} = 2375\ W/m^2$ and $q''_{imp} = 855\ W/m^2$, resulting in initial temperatures of $145°C$ and $74°C$, respectively. An increase of the initial surface temperature increases the removed heat flux, as expected. The main reason is given to the increased temperature difference ΔT between the surface and liquid. However, for $T_0 = 145°C$, nucleation was not observed, meaning that only single-phase heat transfer was achieved.

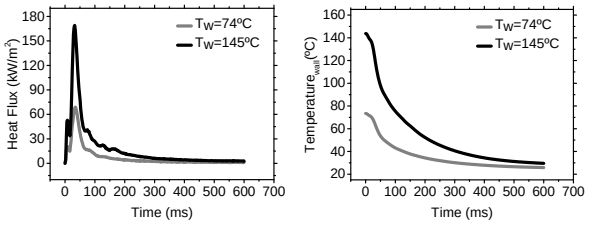

Figure 11: Temporal variation of the heat flux (left) and wall temperature (right) for DI Water (Z=10mm)

4.4.2 Effect of impingement distance

From Figure 12(a), higher impingement distances positively impact the temperature decrease of the surface. This observation is explained by the increase of the cooling area due to the natural droplet dispersion. This behaviour is explicit in Figure 12(b), showing a higher cooling area for Z=20mm.

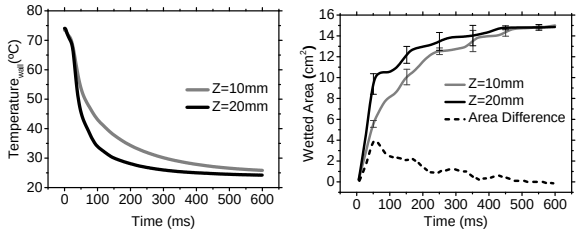

Figure 12: Temporal variation of the wall temperature (left) and wetted cooling area (right) for DI Water

4.4.3 Effect of surface tension and nanoparticles

From Figure 13(a), the decrease of the surface tension speeds up the spray maximum heat flux. This is mainly related to the increase of the wetted cooling area, fig. 13(b), indicating that a lower surface tension diminishes spray development time interval. It should be noted that this promotes the surface temperature decrease, and it is consistent for fluids with similar surface tension values, as fig. 14 depicts.

Regarding the nanoparticle addition, figs. 14 and 15 show the transient cooling curves for the fluids under study. From the three different concentrations of gold spherical nanoparticles, it was expected that higher nanoparticle concentrations should increase the cooling performance.

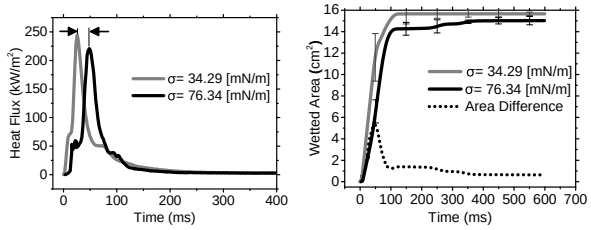

Figure 13: Effect of surface tension on the: Space averaged heat flux (left) and wetted area (right) (T_0=145$^\circ C$, Z=20mm)

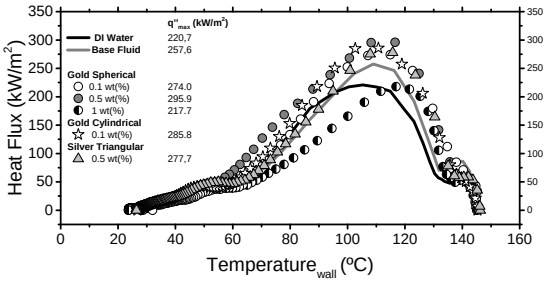

Figure 15: Variation of the overall space averaged heat flux with the space averaged surface temperature

However, the highest concentration performed the worst relative to the lower ones. The one with 0.5 (wt.%) performed better, achieving a maximum heat flux of 295.9 kW/m^2. Nevertheless, this value is only 7.7% higher than the one for 0.1 (wt.%) and indicates that the concentration dependence is not significant within the 0.1 - 1 (wt.%) range.

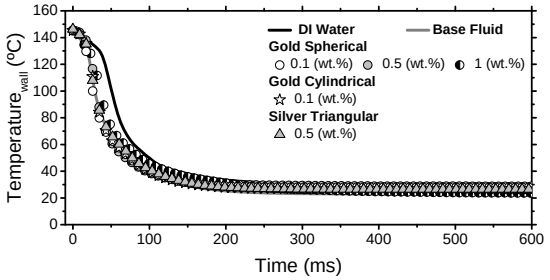

Figure 14: Transient variation of the space averaged surface temperature

Comparing different geometries of gold nanoparticles at the same concentration, no differences are observed. The same happens when changing the nanoparticle base material from gold to silver at 0.5 (wt.%). Nevertheless, the comparable cooling performance between the two materials is consistent with their similar thermal properties (table 1).

As Figure 15 shows, the nanoparticles increased the maximum removed heat flux from the wall at higher temperatures (from $110.8 - 116.6\ ^\circ C$), slightly enhancing cooling performance, at the exception of gold nanospheres at 1(wt.%). Additionally, when computing the heat transfer coefficient as $h = q''_w/(T_w - T_f)$ with $T_f\ = 20\ ^\circ C$, one can calculate the ratios of h_{nf}/h_{BF} or h_{nf}/h_{DW} for different wall temperatures. The nanofluids showed an overall higher heat transfer coefficient when compared to water and the base fluid (water and CTAB). Regarding their h value at q''_{max}, the use of nanofluids resulted in enhancement from 9.8$\%$ to 21.9$\%$ when compared to the base fluid and 11.5$\%$ to 38.8$\%$ when compared with DI water.

Performing a comparison between nanofluids and DI Water, differences are evident. The heat fluxes are lower for DI Water, whose maximum value is given at a lower temperature ($105\ ^\circ C$). Overall. the reason for these differences lye under two major dynamic changes:

- **Spray dynamics** – the lower surface tension caused by the addition of the surfactant promotes the liquid sheet breakup, promoting droplet formation and the occurrence of q"max;
- **Liquid thermal dynamics** – the surfactant increases the surface wettability that promotes the liquid-surface contact, and the nanoparticle addition improves the liquid's thermal conduction.

In this way, the superposition of these two existing dynamics is responsible for the higher cooling performance of the base fluid and consequently of the nanofluids, as opposed to the distilled water. These mechanisms will translate to lower heat transfer coefficients at higher temperatures or on the initial contact with the surface for the DI water spray.

5. Conclusions

The study carried out through this dissertation aimed at describing the heat transfer phenomena that takes place in spray cooling using a new combination of diagnostic techniques. To this end, several nanofluids were atomized, taking advantage of their superior thermodynamic properties, inferring the effects of changing the nanoparticle chemical element, geometry and concentration on the spray dynamics and cooling performance.

Using the phase Doppler anemometer, it was verified that surface tension plays a dominant role in the atomization process. Its value decrease enhances the Weber number that promoted the droplet formation rate, which in turn reduces the overall droplet size. The addition of nanoparticles in the base fluid did not modify the atomization process nor the impact outcomes within this concentration range. This is a positive indicator, meaning that any differences regarding the cooling performance are mainly attributed to heat transfer dynamics at the liquid-solid surface interface.

Afterwards, the experimental installation was adapted to accommodate a heated thin stainless-

steel surface. A high-speed time-resolved infrared camera was placed beneath it to detail the heat transfer and to explore its use to describe these phenomena. Additionally, this camera was synchronized with a high-speed camera that captured lateral images of the spray impacting the surface. This synchronization was helpful to verify the spray actuation repeatability and to examine the different heat transfer mechanisms, although absent. According to the results, this method proved to be reliable as it captured details of the temperature variations from spray impingement. It should also be pointed out that the results were repeatable, mainly attributed to the use of the solenoid valve.

As the surface-to-nozzle distance increased from 10 to 20 mm, the heat flux increased. This is mainly attributed to the increased area that the spray can cover at a higher surface to nozzle distance. Regarding the initial temperature influence, as heat transfer was mainly given through single-phase heat transfer, the removed heat flux increased as the initial temperature increased, as expected. Moreover, the lower surface tension enhanced the transient evolution of the wetted area. This is associated with the decreased droplet contact angle during impact and with the atomization enhancement, which promotes the maximum removed heat flux. Regarding the addition of nanoparticles, within the tested concentrations, no major changes were observed. However, the lowest concentrations of gold nanospheres concentration slightly enhanced the maximum averaged heat flux, which in turn increased the heat transfer coefficient. The opposite was obtained with the highest concentration. Changing their geometry from spheres to cylinders, heat transfer did not express any differences in heat transfer. The same result was obtained for different nanoparticle elements. This shows that these parameters do not influence the heat transfer for this set of concentrations and conditions.

For future studies, it is suggested that the range of nanoparticle concentration should be increased to cause considerate thermophysical changes. Improvements should be made on the heated surface thermal isolation to diminish heat losses, and the imposed heat flux should also increase to trigger two-phase heat transfer mechanisms. It would also be interesting to analyze the surface before and after the nanofluid spray impact to check for nanoparticle deposition.

References

[1] Jungho Kim. Spray cooling heat transfer: The state of the art. *International Journal of Heat and Fluid Flow*, 28(4):753–767, 2007.

[2] Gangtao Liang and Issam Mudawar. Review of spray cooling–part 1: Single-phase and nucleate boiling regimes, and critical heat flux. *International Journal of Heat and Mass Transfer*, 115:1174–1205, 2017.

[3] Ruey-Hung Chen, Louis C Chow, and Jose E Navedo. Effects of spray characteristics on critical heat flux in subcooled water spray cooling. *International Journal of Heat and Mass Transfer*, 45(19):4033–4043, 2002.

[4] Shou-Shing Hsieh, Hsin-Yuan Leu, and Hao-Hsiang Liu. Spray cooling characteristics of nanofluids for electronic power devices. *Nanoscale research letters*, 10(1):139, 2015.

[5] SMS Murshed, KC Leong, and C Yang. Thermophysical and electrokinetic properties of nanofluids–a critical review. *Applied Thermal Engineering*, 28(17-18):2109–2125, 2008.

[6] Munish Gupta, Vinay Singh, Rajesh Kumar, and Z Said. A review on thermophysical properties of nanofluids and heat transfer applications. *Renewable and Sustainable Energy Reviews*, 74:638–670, 2017.

[7] Yanan Gan and Li Qiao. Evaporation characteristics of fuel droplets with the addition of nanoparticles under natural and forced convections. *International Journal of Heat and Mass Transfer*, 54(23-24):4913–4922, 2011.

[8] M Malỳ, AS Moita, J Jedelsky, APC Ribeiro, and ALN Moreira. Effect of nanoparticles concentration on the characteristics of nanofluid sprays for cooling applications. *Journal of Thermal Analysis and Calorimetry*, 135(6):3375–3386, 2019.

[9] Pedro Pontes. Thermographical analysis of interface heat transfer mechanisms, with high temporal resolution. Master's thesis, Universidade de Lisboa Instituto Superior Técnico, 2016.

[10] Shou-Shing Hsieh, Hao-Hsiang Liu, and Yi-Fan Yeh. Nanofluids spray heat transfer enhancement. *International Journal of Heat and Mass Transfer*, 94:104–118, 2016.

[11] Ji-Hwan Lee, Kyo Sik Hwang, Seok Pil Jang, Byeong Ho Lee, Jun Ho Kim, Stephen US Choi, and Chul Jin Choi. Effective viscosities and thermal conductivities of aqueous nanofluids containing low volume concentrations of al2o3 nanoparticles. *International Journal of Heat and Mass Transfer*, 51(11-12):2651–2656, 2008.